

ACCEPTANCE TESTING OF TUNGSTEN-CFRP LAMINATE INTERFACES FOR SATELLITE ENCLOSURES

M. Kanerva¹, J. Jokinen¹, P. Antunes², M. Wallin¹, T. Brander¹, O. Saarela¹

¹Department of Applied Mechanics, School of Engineering, Aalto University
P.O. Box 14300, FI-00076 Aalto, Finland
Email: mikko.kanerva@aalto.fi, web page: <http://www.aalto.fi/en>

²Instituto de Telecomunicações and Department of Physics, University of Aveiro
3810-193 Aveiro, Portugal
Email: pantunes@av.it.pt, web page: [http://www. https://www.ua.pt](http://www.https://www.ua.pt)

Keywords: Hybrid laminates, Interface, Space structure, Surface treatment

ABSTRACT

Lightweight electronics housings for satellites are multi material systems and can provide efficient radiation protection. The challenge in hybrid concepts consisting of carbon fibre reinforced plastic (CFRP) and tungsten (W) is that the adhesion of CFRP onto rolled tungsten foils is not reliable. After manufacture, the interface between tungsten and the matrix polymer is loaded by residual stresses due to the high Young's modulus difference and thermal expansion mismatch. In this study, we analyse a three-point bending (3PB) method for acceptance testing of interfaces in W-CFRP laminates with the help of finite element analysis (FEA). Our results showed that the 3PB test method introduced here was capable of distinguishing between different tungsten surface treatments. Also, the scatter in critical force values and apparent shear strengths was low compared to pull-off testing. The FEA indicated that brittle interfacial failure initiates at the specimen free edges and that the propagation of the failure causes a clearly observable peak in the force-deflection curves.

1 INTRODUCTION

Sensitive electronics in satellites are protected by enclosures. In space environment, different systems and structures face intensive radiation including electron, proton, as well as alpha and beta particle bombardment [1,2]. The lightest protective enclosures are built of polymer matrix composites.

The attenuation of the radiation by electrons in lightweight enclosures is realized by laminating thin layers of refractory metal such as tungsten into the laminate [3,4]. The challenge in this type of hybrid laminate concepts, where carbon fibre reinforced plastic (CFRP) and tungsten foils are applied, is that the adhesion between the CFRP layers and rolled tungsten foils is not mechanically reliable [5]. Not too many surface treatments have been developed for tungsten and the satellite application restricts the selection of treatments. For example, the following issues can easily limit the surface treatment selection:

- Tungsten foils are very thin ($\approx 50 \mu\text{m}$) and must not be penetrated by a surface treatment.
- A treatment shall not drastically change the layer composition, thickness, and density.

The curing of a tungsten-CFRP laminate at an elevated temperature results in residual stresses due to the thermal expansion mismatch between CFRP and tungsten. On a micro-scale, the interface is extremely stressed due to the high Young's modulus difference between tungsten and the matrix polymer. For the latest enclosure designs, asymmetric composite lay-ups can be implemented in order to maximise radiation protection features and, at the same time, minimise laminate distortions due to residual stresses [6].

To develop viable surface treatments for tungsten-CFRP hybrids in modern satellite projects, a proper test method for adhesion must be established. In this, the method must be able to show the

effects of different surface treatments. In addition, the test method must be enough robust to enable fast execution and analysis when numerous surface treatment candidates are being evaluated. It should be noted that present test methods do not consider the effect of residual stresses not to mention the effect of ply-orientation and the stacking sequence of composite and metal layers. In this study, we analyse a three-point bend test method for acceptance testing of tungsten-CFRP laminate interfaces. We focus on the correct observation of failure of the tungsten-CFRP interface. Our study includes an experimental part and a numerical simulation part. First, we analyse the experimental results of flexural tungsten-CFRP specimens. Second, we develop finite element models capable of interfacial crack propagation simulation.

2 EXPERIMENTAL PROCEDURE AND NUMERICAL PROBLEM FORMULATION

2.1 Specimen preparation

Tungsten (W) was applied in the form of rolled foils (nominal thickness 50 μm , purity 99.95%) provided by Alfa Aesar (Germany). CFRP was applied in the form of unidirectionally reinforced pre-preg tape (nominal thickness 0.29 mm, aerial weight 300 g/m^2 , fibre content 68% weight/weight) provided by Advanced Composites Group (UK). The pre-preg consisted of MTM[®] 57 toughened epoxy resin (ACG, UK) and M40J(12K) high-modulus carbon fibres (Toray, USA).

Two different specimen series were prepared. For the first series, a chemical etching treatment (HFNS) was applied to a tungsten foil. HFNS is a pure chemical treatment involving optimised degrease steps by solvents, a hydrofluoric-nitric-sulphuric-acid immersion step, proper rinsing steps, and finally dehydration. Details of the HFNS treatment and the resulting effects on tungsten (oxide layer) and adhesion have been reported in our previous studies [4,5]. For the second specimen series, a gradient copper-nickel-gold (Cu-Ni-Au) coating was applied to another tungsten foil. The gradient coating was designed and manufactured by Eforit Oy (Finland). The coating was specifically tailored for tungsten. The coating was deposited by combining electrolytic and electroless deposition techniques [7]. Prior to the actual coating process, the foil was degreased using methyl-ethyl-ketone (MEK). An atomic-level gold layer was deposited first. The final thickness of the tri-layer coating amounted to 3-5 μm . Details of the Cu-Ni-Au coating and the resulting effects on adhesion have been reported in our previous study [5].

The W-CFRP test specimens were laminated by applying a stacking sequence $[0_{14}/W/0_7]$. Two layers of polyamide peel ply were placed between the upper and lower halves of two-piece silicone moulds to absorb any overflow resin. In this study, the specimens were laminated individually inside the silicone moulds. In this way, no cutting of specimens was needed. Hence no damage due to cutting was induced at the specimen free edges. The silicone moulds with the specimens were vacuum bagged using a large polyamide briefcase bag (0.95 bar vacuum). The specimens were cured according to the pre-preg manufacturer's instructions (60 min hold at 120 °C). The size of each W-CFRP specimen after the cure was (width \times length \times thickness) 19 mm \times 39 mm \times 6 mm.

2.2 Three-point bend (3PB) test

A three-point bend test fixture was attached to a hydraulic testing machine (100 kN). The radius of the loading nose in each support was 3.0 mm. In between the two lower supports (loading nose separation 34 mm), a laser displacement transducer (LK-081, Keyence, Japan) was mounted to measure the deflection of a specimen during testing. To achieve a high intensity laser reflection from CFRP, a thin gold coating was sputtered on each specimen's back surface prior to testing (sputtering temperature 25-40 °C). Also, white typewriter's correction paint was applied on the sides of each specimen to make observations of failure modes. The testing machine was displacement-controlled (0.3 mm/min) using servo-hydraulic, computerized control (Multipurpose Elite, MTS, USA). A description of the test setup is shown in Fig. 1. The CFRP portion with 14 layers was always set against the lower supports and, five specimens per each test series were tested.

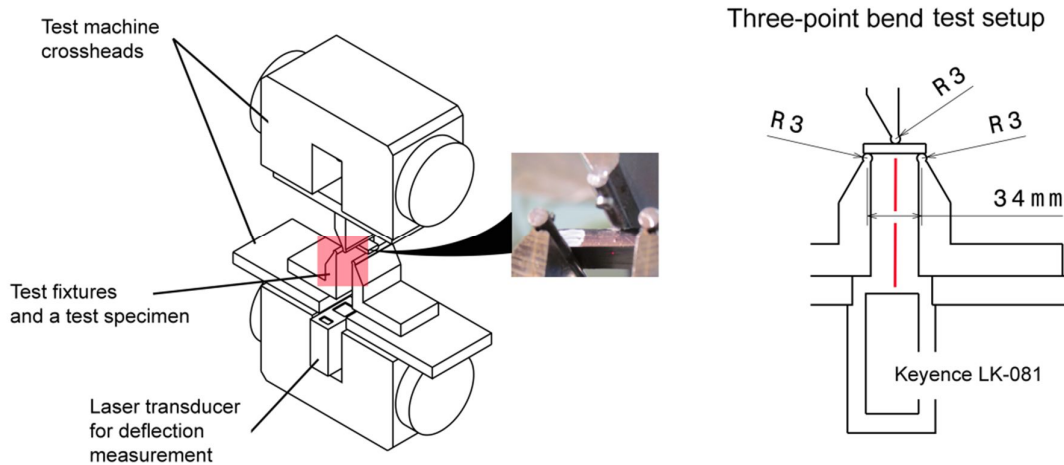


Figure 1: Description of the 3-point bend setup for testing of laminated W-CFRP specimens.

2.3 Finite element (FE) modelling and 3PB test simulation

2.3.1 General model description

A commercial finite element (FE) code Abaqus 6.14-2 was used for modelling and simulation of the 3PB testing. The entire model consisted of a test specimen, upper steel support (loading nose) and an analytical rigid surface representing the two lower supports. The test specimen alone was built of four parts:

- (1) Tungsten foil,
- (2,3) CFRP parts above and below the tungsten foil, and
- (4) Thin CFRP part having a thickness of 0.1 mm and located against the tungsten foil.

The separate parts of the test specimen were attached primarily using rigid (tie) constraints. It should be noted that the tungsten foil is very thin (50 μm) and the element aspect ratio was intended to keep close to unity. The separate parts allowed independent element meshes; the thin CFRP was used to have mesh equivalence at the interface for interface failure analyses. The model consisted of 56 593 elements and the overall element mesh is illustrated in Fig. 2. The material properties applied to the model are shown in Table 1.

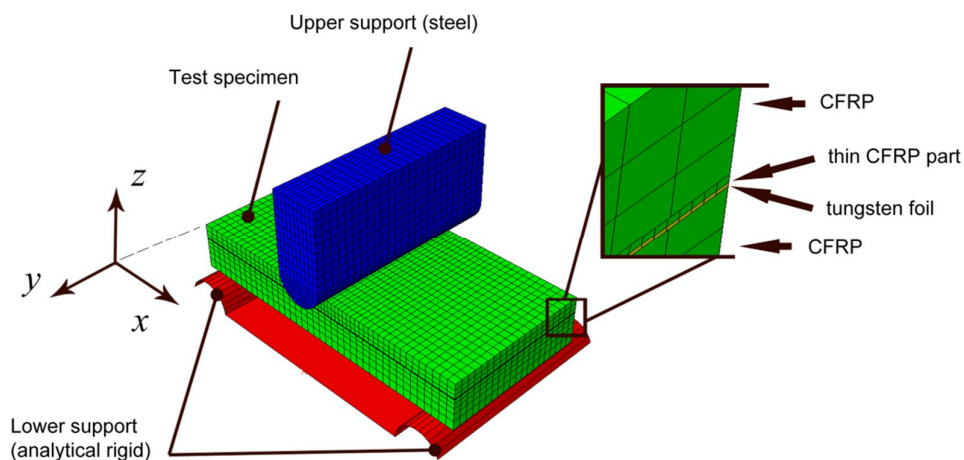


Figure 2: The finite element model used for simulating a 3PB test designed for W-CFRP specimens.

Each of our simulation was performed in two separate steps. The first step introduced a temperature change of $\Delta T = -100$ °C to account for residual stresses. In the second step, the upper support was displaced vertically against the specimen in order to bend it. The reaction force was recorded in the upper support to determine the force (F) needed to counteract the specimen's flexural stiffness. The rigid body motion of the test specimen was restricted using appropriate boundary conditions per step.

Engineering constant		CFRP	Steel	Tungsten
E_x	[GPa]	191.5	210	410
E_y, E_z	[GPa]	6.3	210	410
ν_{xy}	–	0.31	0.3	0.28
G_{xy}, G_{yz}, G_{xz}	[GPa]	7.2	(80.7)	(160.2)
α_{xx}	[1/°C]	$-0.43 \cdot 10^{-6}$	–	$4.5 \cdot 10^{-6}$
α_{yy}, α_{zz}	[1/°C]	$44.0 \cdot 10^{-6}$	–	$4.5 \cdot 10^{-6}$

Table 1: Material properties used for modelling the 3PB test setup and W-CFRP specimen.

2.3.2 Interface failure model

The failure of the tungsten-CFRP interface was simulated using two different numerical methods. First, the Virtual Crack Closure Technique (VCCT) (see e.g. [8]) was used to estimate the strain energy, which could be released by brittle fracture. For this, three different symmetric pre-cracks were considered as described in Fig. 3. The extent (length) of the pre-cracks was also considered. Strain energy release rates (SERR) were recorded when the displacement reached a critical level defined by the 3PB tests. The crack was not propagated when using the model with the VCCT implementation.

Second, cohesive elements (see e.g. [9]) were implemented for a model to simulate the failure of the entire tungsten-CFRP interface, i.e., crack initiation and propagation. In total 4704 cohesive elements with zero thickness were placed along the interface between the tungsten foil and the thin CFRP part. A bi-linear traction-separation law was presumed for interfacial failure. The slope of the first linear part was set to $1 \cdot 10^{15}$ N/m³ and three different values (75 MPa, 85 MPa, 95 MPa) were considered for the maximum scalar stress (namely maximum traction or cohesive strength). This scalar stress value was defined by a quadratic stress criterion. The area enclosed by the bi-linear traction-separation curve represents the energy release required for the modelled interfacial bond to break and was estimated based on the simulations using the model with the VCCT implementation. A one-fourth FE model was created for efficient computation using the model with the cohesive elements.

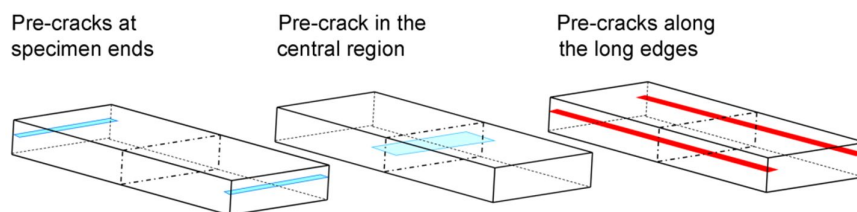


Figure 3: Three different pre-cracks considered for an FE model with the VCCT implementation.

3 RESULTS AND ANALYSIS

3.1 3PB test experiment results and analysis

Typical failure modes observed in the W-CFRP specimens are shown in Fig. 4(a). By visual observation, the failure at the tungsten-CFRP interface seemed to occur chronologically first. However, the typical interfacial cracks as well as interlaminar cracks extended only halfway through a specimen. Suggested behaviour of the specimen due to interfacial failure is illustrated in Fig. 4(b).

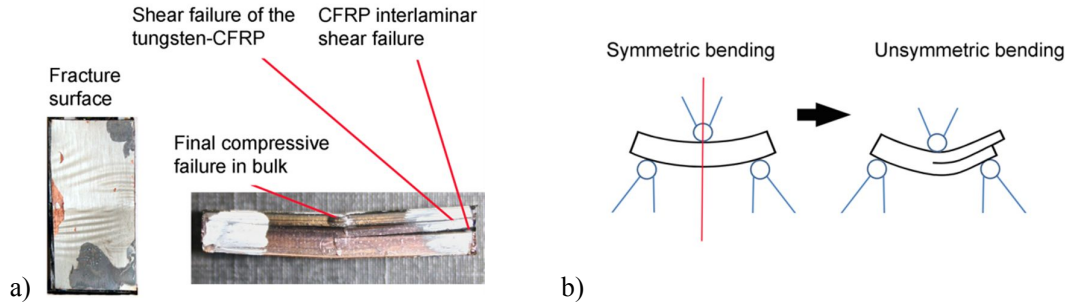


Figure 4: Visual observations: (a) fracture surface and different failure modes shown on the side of a specimen; (b) suggested deformation shape after shear failure halfway through a specimen.

The recorded force-time curves for the two specimen series are shown in Fig. 5. Each recorded force curve indicated a clearly distinguishable peak load, after which a drastic reduction in the measured load appeared. The peaking in the force data presumably represented the failure of the tungsten-CFRP interface and the subsequent reduction in the specimen's flexural stiffness. However, the first observed peak did not represent the maximum load (maximum compressive force) for the specimen no^o 1 of the HFNS series and specimen no^o 2 of the Cu-Ni-Au series.

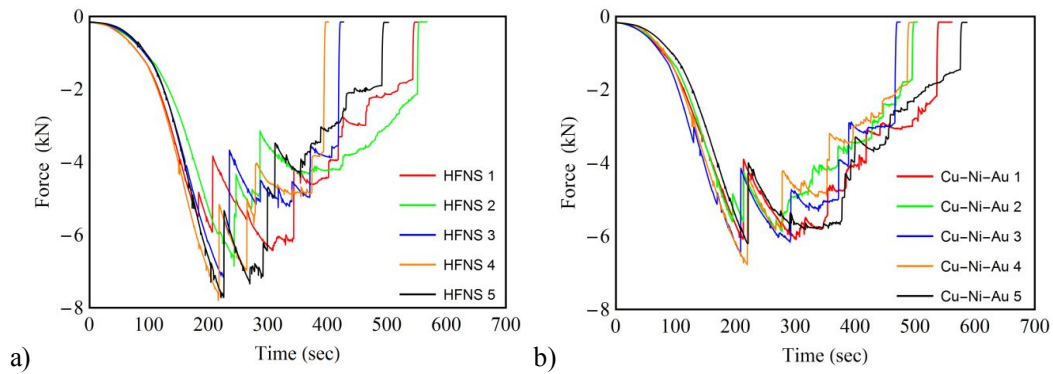


Figure 5: Force-time curves measured during 3PB testing of W-CFRP specimens: (a) HFNS treatment applied on the tungsten foils; (b) Cu-Ni-Au coating applied on the tungsten foils.

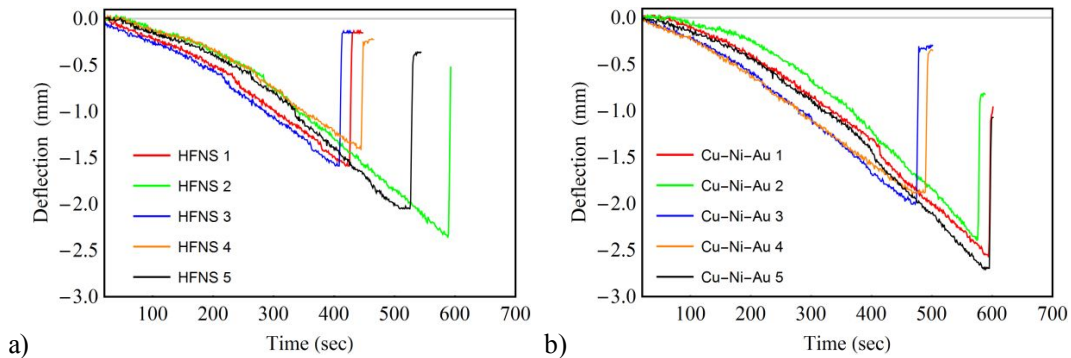


Figure 6: Deflection-time curves measured during 3PB testing of W-CFRP specimens: (a) HFNS treatment applied on the tungsten foils; (b) Cu-Ni-Au coating applied on the tungsten foils.

The measured deflection-time curves for the two specimen series by the laser transducer are shown in Fig. 6. It can be seen that the deflections did not represent linear functions of time, which again

indicates that the deformed shape of a specimen (or a delaminated part of it) changes during the testing. For most of the specimens, the deflection-time curves seemed rather bi-linear. It was found that the first part was essentially linear, as shown by a least-squares fitted line in Fig. 7(a). By plotting the force and deflection data together against time, it can be seen that the sudden slope change in the deflection curves emerged simultaneously with the first peak loads (see Fig. 7(b)).

Using linear approximation for the laser transducer data prior to the peak load, force-displacement curves were determined and are shown in Fig. 8. It can be seen that the behaviour of the HFNS series specimens was relatively constant (in terms of flexural stiffness). In contrast, the Cu-Ni-Au series introduced more scatter (in terms of flexural stiffness). Variation in the flexural stiffness, as well as small discontinuities in the curves until the first peak load, suggests that the tungsten-CFRP interface might fail progressively in the case of Cu-Ni-Au coating on tungsten.

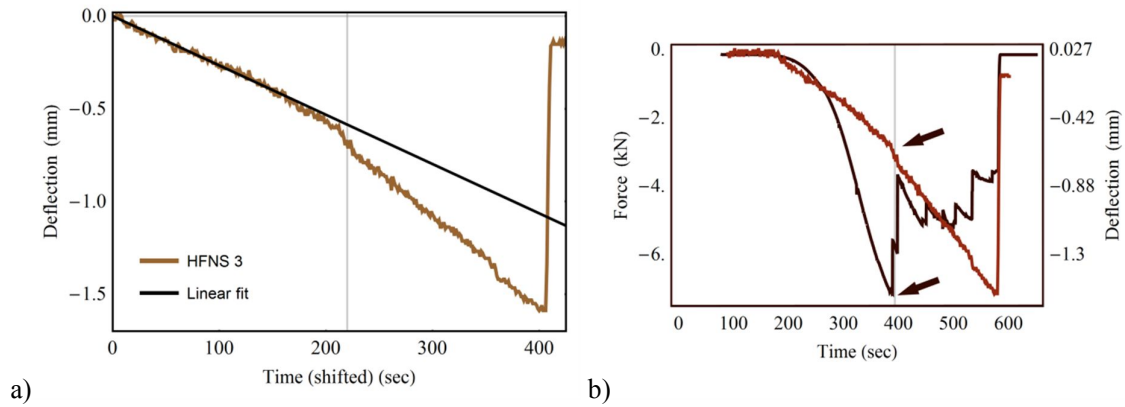


Figure 7: Critical force and deflection analysis: (a) least squares fitting of a line until a slope change; (b) typical force and deflection data plotted against time. Arrows show the point of first major failure.

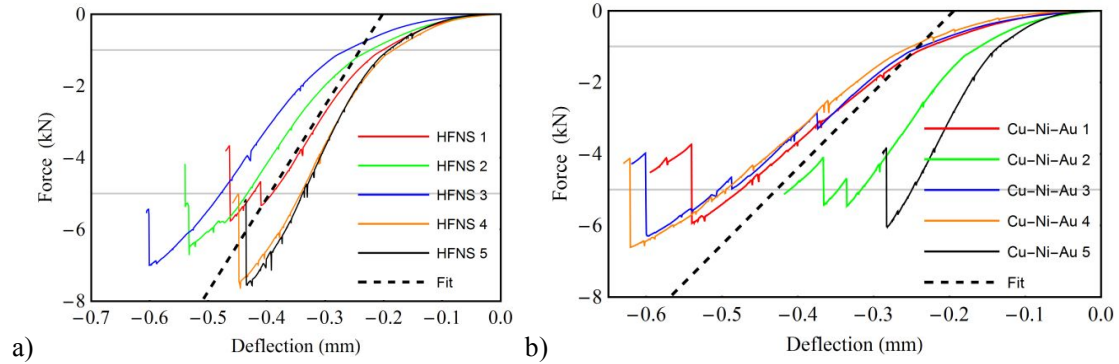


Figure 8: Force-deflection curves determined from 3PB test data: (a) HFNS treatment applied on tungsten; (b) Cu-Ni-Au coating applied on tungsten. The fittings are based on a force range -5...-1 kN.

The specimens where the HFNS treatment was applied on tungsten had an 11.2% higher failure load (compared to the Cu-Ni-Au coating), which suggests better adhesion of CFRP to the HFNS treated tungsten foils. An estimate of the adhesion can be made using standard methods for calculating apparent shear strength (τ_A). Standard test methods for short beam strength of fibre-reinforced composite specimens present the following equation [10,11,12]:

$$\tau_A = 0.75 F_u / (t \cdot w), \quad (1)$$

where F_u is the critical force, t is the specimen thickness and w is the specimen width.

Tungsten surface treatment	Average peak force [kN]	Average deflection at peak force [mm]	Approximate flexural stiffness [kN/mm]	Apparent shear strength [MPa]
<i>HFNS</i>	-6.922 ± 0.920	-0.570 ± 0.054	25.9	46.5 ± 5.7
<i>Cu-Ni-Au</i>	-6.224 ± 0.438	-0.669 ± 0.085	21.4	41.1 ± 3.0

Table 2: Peak load and corresponding deflection values (average \pm standard deviation), and flexural stiffness based on linear fitting (average \pm standard deviation), determined from the 3PB test data of W-CFRP specimens and two different tungsten surface treatments.

The calculated apparent shear strengths for the specimens in this study are given in Table 2. The specimen where the HFNS treatment was applied on the tungsten foils had 13.1% higher apparent shear strength compared to the Cu-Ni-Au coating. In comparison, the results of the pull-off testing in our previous study [5] indicated 14.0% *lower* adhesion for the HFNS treatment. However, the (average) pull-off results were accompanied by very high standard deviation (47%) as well as high variation in the failure mode [5]. Using the 3PB test method introduced here, the standard deviations were clearly lower for the critical force (13% for the HFNS series and 7% for the Cu-Ni-Au series). Moreover, the standard deviations were low for the apparent shear strength (12% for the HFNS series and 7% for the Cu-Ni-Au series). It should be noted that Eq. 1 presumes the specimen failing along the neutral axis and that the specimen is layer-wise homogenous. In this study, the exact shear strength over the entire failure plane will be analysed using finite element analysis.

3.2 Simulated flexural stiffness during 3PB

The effect of the finite element type on the flexural stiffness is shown in Fig. 9. In general, the simulated flexural stiffness corresponded well with the experiments (29.7 kN/mm, using C3D8I elements). The linear C3D8I element type (incompatible modes applied) provided the highest flexural stiffness and efficient computation. In contrast, the reduced-integrated C3D8R element type provided the lowest stiffness. For a quadratic C3D20R element type, the initial behaviour was stiffer when compared to all other element types. The meshing (doubling of elements in the tungsten foil's thickness direction or quadratic elements in the load nose) did not have significant effect on the flexural stiffness. The C3D8I elements were selected for further simulations.

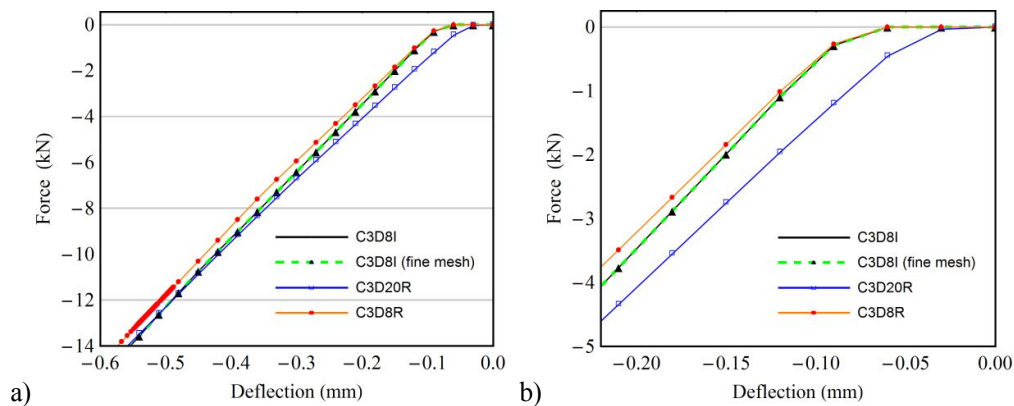


Figure 9: The effect of element type on the simulated flexural stiffness of a W-CFRP FE model: (a) data presented over a force range 0...-14 kN; (b) data zoomed over a force range 0...-5 kN.

3.3 FE stress analysis of W-CFRP laminate specimens

A stress analysis was performed to study the risk of bulk failure during the 3PB test and also to study the distribution of shear stress along the tungsten-CFRP interface. Based on the analysis, the

bulk failure in CFRP is most potential under the upper support (loading nose), as shown by the von Mises stress distribution in Fig. 10(a). In Fig. 10(a), the reference (upper limit) is an experimental tensile stress to failure determined for the CFRP used (1701 MPa). However, even the highest stress value (1150 MPa) has 32% marginal to the experimental reference (at a load corresponding to interfacial failure). Interestingly, the distribution of longitudinal stress (σ_{xx}) in the tungsten foil forms waves, as illustrated in Fig. 10(b). These stress waves are a direct consequence of the residual stresses and the respective deformed, non-flat shape prior to bending of the specimen. The shear stress distribution in the vicinity of the tungsten-CFRP interface is rather constant through the width of the specimen – the highest shear stress at the interface amounts to ≈ 56 MPa.

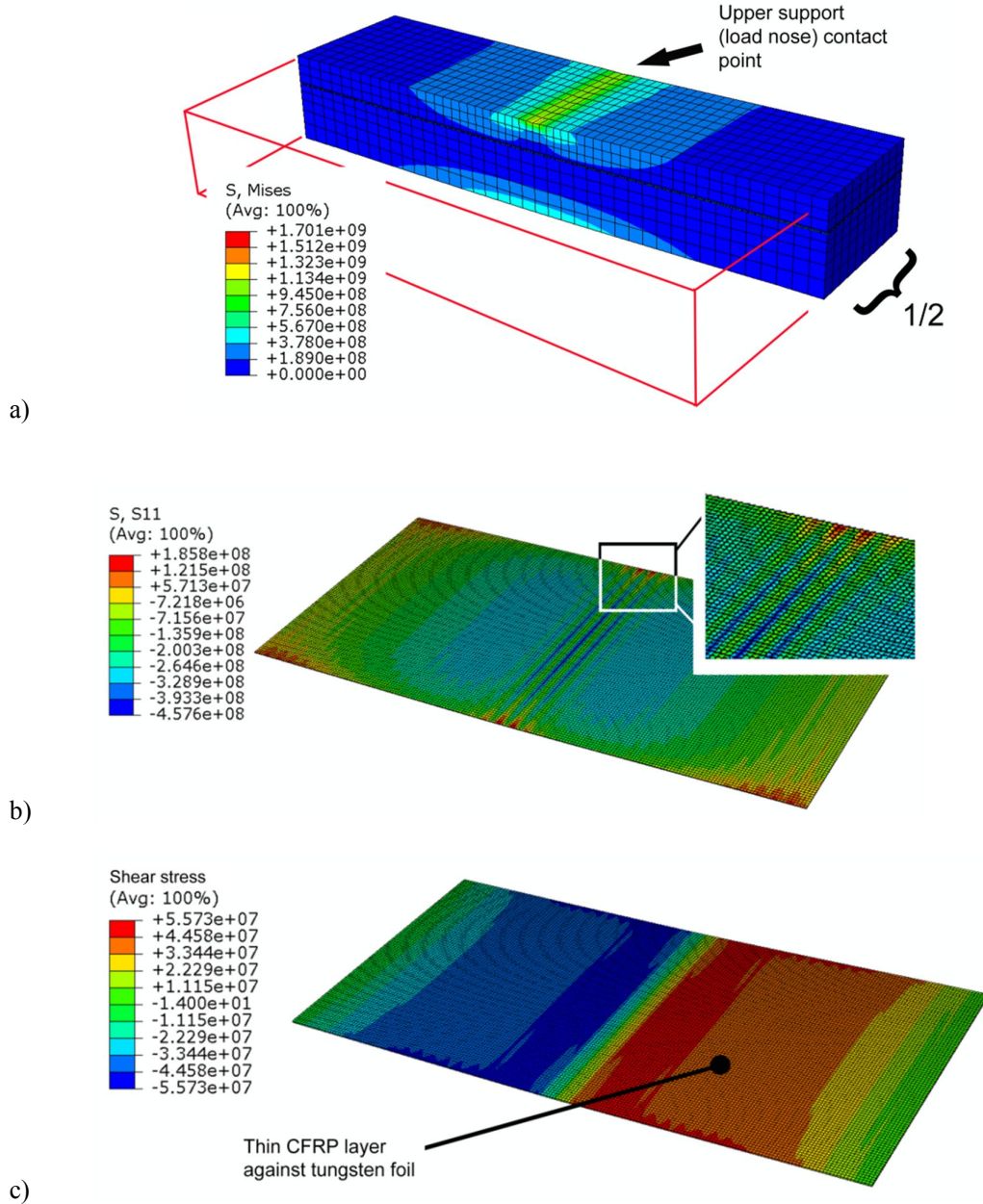


Figure 10: Simulated 3PB test at a load level $F = -7.3$ kN: (a) outer and internal von Mises stress distributions; (b) longitudinal stress component ($\sigma_{xx} = S11$) in the tungsten foil; (c) shear stress distribution in the thin CFRP part adjacent to the W-CFRP interface.

3.4 Strain energy release rate (SERR) analysis

Firstly, for all of the modelled pre-cracks (described in Fig. 3), the highest SERR values emerged along the free edges of the W-CFRP specimen and not inside the specimen. This result is due to the finite element mesh generation, residual stresses and the resulting free-edge stresses. The SERR values per crack-tip loading mode and recorded in the points giving the highest values (at free edge), are given as a function of loading in Figs. 11-13. The increase in mode II SERR as a function of load was surprisingly low for all of the modelled pre-cracks. For the pre-crack in the central region (Fig. 12), the mode II component increases significantly for a very high loading and presuming a large pre-crack (1.6 mm pre-crack extent, Fig. 12(b)). Mode I components *decreased* monotonically for all of the pre-cracks as the loading was increased. However, the mode I SERR values *prior to loading* were high due to the high residual stresses in the specimen. Also, the effect of the extent of pre-crack was pronounced for mode I crack tip loading. These results suggest that the mode I crack tip loading leads to the initiation of the interfacial failure. The third, twisting crack tip loading mode (mode III) had relatively high values (60...111 J/m²) for small regions (corners of the pre-crack) yet it was presumed highly dependent on the free-edge stresses and meshing effects.

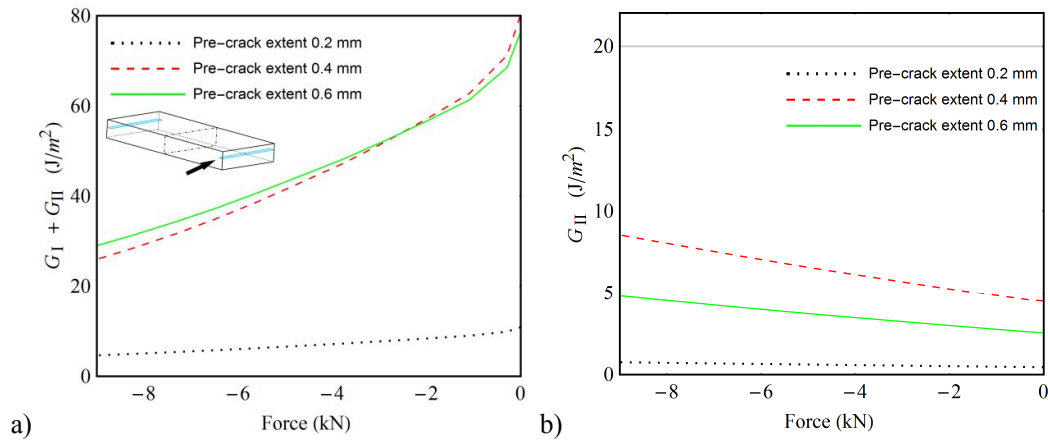


Figure 11: Simulated strain energy release rate using an FE model with VCCT implementation and a pre-crack placed in both ends of a specimen: (a) sum of mode I and mode II SERR components as a function of force during 3PB; (b) mode II SERR component as a function of force during 3PB.

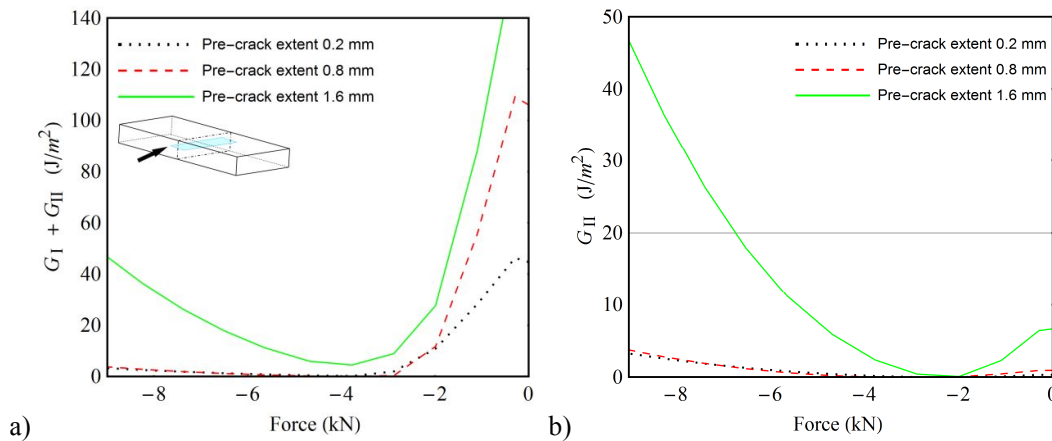


Figure 12: Simulated strain energy release rate using an FE model with VCCT implementation and a pre-crack placed centrally inside a specimen: (a) sum of mode I and mode II SERR components as a function of force during 3PB; (b) mode II SERR component as a function of force during 3PB.

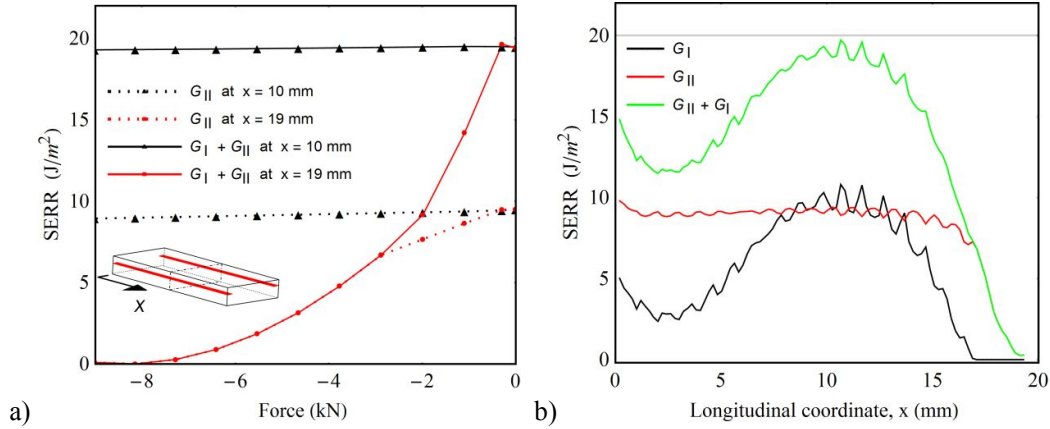


Figure 13: Simulated strain energy release rate using an FE model with VCCT implementation and pre-cracks placed along both long edges of a specimen: (a) mode I and mode II SERR components in two points as a function of force during 3PB; (b) mode I and mode II SERR components and their sum as a function of longitudinal coordinate (at a load level $F = -7.3$ kN).

Pre-cracks placed along the both long edges of a specimen were simulated to understand how the maximum SERR values, which were found to occur at the long free edge, are distributed between the lower and upper support. Interestingly, the determined spatial SERR distribution for a pre-crack along the long edge was far from linear not to mention constant, as shown in Fig. 13. As a conclusion, the SERR analysis suggested the following: (1) the interfacial failure initiates along the long free edges of the W-CFRP specimens and, (2) the interfacial failure is prone to grow along the long edges and propagate towards the central region on the interface. In other words, the growth of interfacial failure is most probable for points at $x \approx 10$ mm and not under the upper support nose ($x \approx 19$). Based on the simulations, the critical SERR values were suggested to range from 30 J/m^2 to 100 J/m^2 and from 5 J/m^2 to 40 J/m^2 for mode I and mode II, respectively.

3.5 Simulated interfacial failure during 3PB testing

The simulation using a model with cohesive elements confirmed that the interfacial failure initiates at the specimen's longitudinal edges. Graphical presentation of the failure initiation and propagation along the cohesive element plane between the tungsten foil and the thin CFRP part is illustrated in Fig. 14. The initiation and progression of the interfacial failure was fast and led to immediate decrease in loading as shown in Fig. 15(a). The selected magnitude of the maximum scalar stress (i.e. cohesive strength, $\bar{\sigma}$) was found to significantly affect the critical force and the amount of immediate decrease. Three different $\bar{\sigma}$ values were considered; a range $\bar{\sigma} = 85 \dots 95$ MPa was found to produce results, which were in proper agreement with the experimental failure initiation. The simulated flexural stiffness was in excellent agreement with the experimental results.

The interlaminar failure of the CFRP part was also simulated. A cohesive element plane was constructed at the neutral plane of the specimen. Literature data [9] of a comparable CFRP material was used to implement a bi-linear traction-separation law for the CFRP interlaminar failure. The traction-separation law for the tungsten-CFRP interface was applied according on the previous simulation (see Fig. 15(a), $\bar{\sigma} = \bar{\sigma}_w = 85$ MPa). The initial simulation results, shown in Fig. 15(b), showed that the first peak in the force-deflection curve emerged due to the failure of the tungsten-CFRP interface. The interlaminar failure of the CFRP caused another clear drop in the force-deflection curve and occurred subsequent to the failure of the tungsten-CFRP interface. The simulated force-deflection behaviour helped to identify the point of interfacial failure at the tungsten-CFRP interface from experimental data.

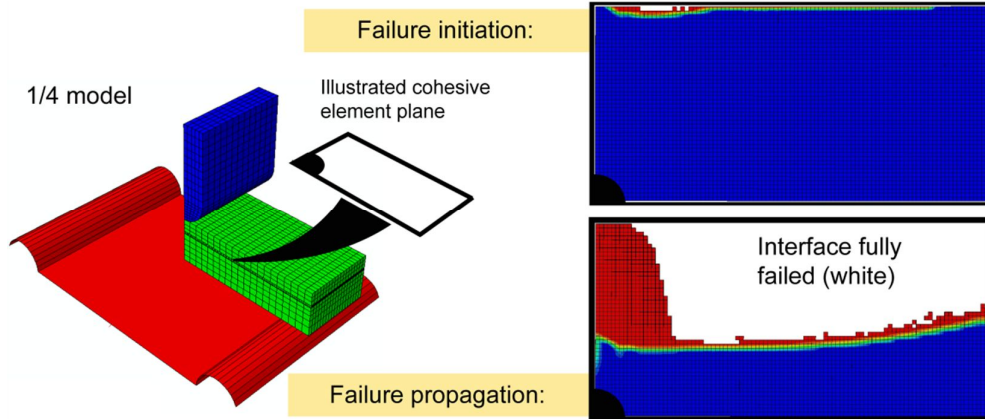


Figure 14: Simulated 3PB testing using a model with cohesive elements. A one-fourth model was used in the simulation and the effect of cohesive strength was studied by considering three different values ($\bar{\sigma} = 75 \text{ MPa} / 85 \text{ MPa} / 95 \text{ MPa}$, $G_{Ic} = 40 \text{ J/m}^2$, $G_{IIc} = 40 \text{ J/m}^2$, $G_{IIIc} = 10\,000 \text{ J/m}^2$).

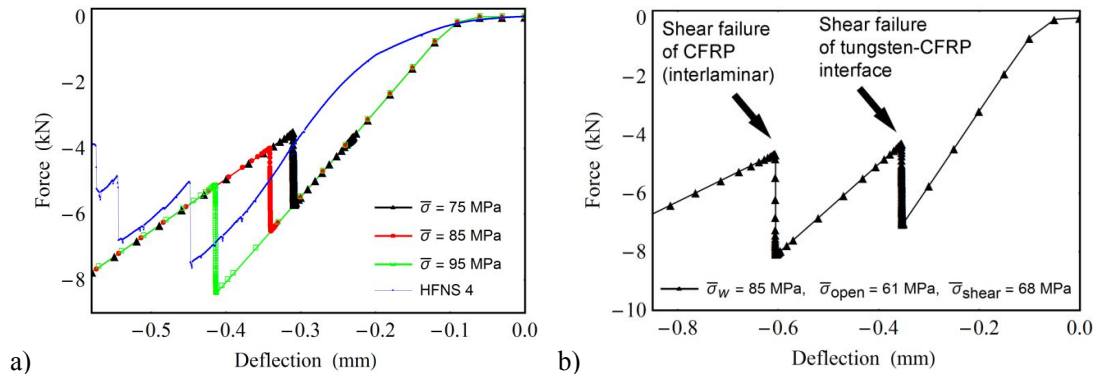


Figure 15: Simulated force-deflection behaviour of a 3PB test model with cohesive elements: (a) cohesive elements only at the W-CFRP interface; (b) cohesive elements at the W-CFRP interface and also at the neutral plane in order to simulate interlaminar failure of the CFRP part (for CFRP: $\bar{\sigma}_{open} = 61 \text{ MPa}$, $\bar{\sigma}_{shear} = 68 \text{ MPa}$, $G_{Ic} = 75 \text{ J/m}^2$, $G_{IIc} = 547 \text{ J/m}^2$, $G_{IIIc} = 10\,000 \text{ J/m}^2$).

9 CONCLUSIONS

In this work, acceptance testing of interfaces in tungsten-CFRP radiation shielding materials was studied. A three-point bend (3PB) test method was introduced and applied on two different laminated specimen series and two different tungsten surface treatments. The validity of the identification of interfacial failure from experimental data was studied using finite element analysis (FEA). The results showed that the 3PB test method is capable of distinguishing between laminate specimens where different tungsten surface treatments have been applied. Additionally, the scatter in critical force values and calculated apparent shear strength values is low compared to pull-off testing (see e.g. [5]). However, in the event of possible progressive and ductile interfacial failure, it could be difficult to determine a single load peak representative of the interfacial failure. The results of the FEA indicated that brittle interfacial failure initiates at the specimen's long (free) edges and that the propagation of the failure causes a clearly observable peak in the force-deflection curves – validating the experimental force peak representative of the tungsten-CFRP interfacial failure.

ACKNOWLEDGEMENTS

The research leading to these results has received funding from the European Community's Seventh Framework Programme (FP7/2007-2013) under Grant Agreement 262746. The authors want to gratefully acknowledge CSC IT Center for Science for their computation services.

REFERENCES

- [1] R. Mangeret, T. Carrière and J. Beaucour, Effects of material and/or structure on shielding of electronic devices, *IEEE Transactions Nuclear and Plasma Sciences*, **43**(6),1996, pp. 2665–2670 ([doi: 10.1109/23.556851](https://doi.org/10.1109/23.556851)).
- [2] G. Atxaga, J. Marcos, M. Jurado, A. Carapelle and R. Orava, Radiation shielding of composite space enclosures, *Proceedings of the 63rd International Astronautical Congress 2012 (Eds. K. Fletcher), Naples, Italy, October 1-5, 2012*, International Astronautical Federation, Paris, France, ISBN: 978-1-62276-979-7.
- [3] T. Brander, K. Gantois, H. Katajisto and M. Wallin, CFRP electronics housing for a satellite, *Proceedings of the 9th International Conference on Spacecraft Structures, Materials and Environmental Testing 2005 (ESA SP-581) (Ed. K. Fletcher), Noordwijk, The Netherlands, May 10-12, 2005*, ESA ESTEC, Noordwijk, The Netherlands, ISBN: 92-9092-892-1.
- [4] M. Kanerva, L.-S. Johansson, J.M. Campbell, H. Revitzer, E. Sarlin, T. Brander and O. Saarela, Hydrofluoric-nitric-sulphuric-acid surface treatment of tungsten for carbon fibre-reinforced composite hybrids in space applications, *Applied Surface Science*, **328**, 2015, pp. 418-427 ([doi: 10.1016/j.apsusc.2014.12.036](https://doi.org/10.1016/j.apsusc.2014.12.036)).
- [5] M. Kanerva, J.R. Koerselman, H. Revitzer, L.-S. Johansson, E. Sarlin, A. Rautiainen, T. Brander and O. Saarela, Structural assessment of tungsten-epoxy bonding in spacecraft composite enclosures with enhanced radiation protection, *Proceedings of the 13th International Conference on Spacecraft Structures, Materials and Environmental Testing 2014 (ESA SP-727) (Ed. L. Ouwehand), Braunschweig, Germany, April 1-4, 2014*, ESA ESTEC, Noordwijk, The Netherlands, ISBN: 978-92-9221-291-9.
- [6] J.R. Koerselman, *A Multidisciplinary Optimization of Composite Space Enclosures*, Master's thesis, Delft University of Technology, Department of Aerospace Design, Integration & Operations, Delft, The Netherlands, 2012 ([uuiid: 9c81ea64-37a4-4781-9247-2d42cb439e19/](https://doi.org/10.1016/j.apsusc.2014.12.036)).
- [7] Eforit Oy, Finland. Plating Techniques (2015) <<http://eforit.fi/en/plating/plating-techniques/>>
- [8] R. Krueger, Virtual crack closure technique: History, approach and applications, *Applied Mechanics Review*, **57**, 2004, pp. 109-143 ([doi: 10.1115/1.1595677](https://doi.org/10.1115/1.1595677)).
- [9] A. Turon, Simulation of delamination in composites under quasi-static and fatigue loading using cohesive zone models, Doctoral thesis, University of Girona, Spain, 2006.
- [10] EN 2563, *Aerospace series – Carbone fibre reinforced plastics – Unidirectional laminates – Determination of the apparent interlaminar shear strength*, European Standard, CEN European Committee for Standardization, Brussels, Belgium, 1997.
- [11] BS EN ISO 14130, *Fibre-reinforced plastic composites – Determination of apparent interlaminar shear strength by short-beam method*, British Standards Institution, BSI, London, United Kingdom, 1998.
- [12] D 2344, *Standard Test Method for Short-Beam Strength of Polymer Matrix Composite Materials and Their Laminates*, ASTM, West Conshohocken, United States, 2000.